Biogeochemistry (2023) 162:25–42
https://doi.org/10.1007/s10533-022-01012-9

BIOGEOCHEMISTRY LETTERS

Using fixed-potential electrodes to quantify iron and manganese redox cycling in upland soils

Caitlin Hodges · John M. Regan · Brandon Forsythe · David Oakley · Jason Kaye · Susan L. Brantley

Received: 1 February 2022 / Accepted: 22 December 2022 / Published online: 12 January 2023

Abstract Although metal redox reactions in soils can strongly affect carbon mineralization and other important soil processes, little is known about temporal variations in this redox cycling. Recently, potentiostatically poised electrodes (fixed-potential electrodes) have shown promise for measuring the rate of oxidation and reduction at a specific reduction potential in situ in riparian soils. Here for the first time, we used these electrodes in unsaturated soils to explore the fine-scale temporal redox fluctuations of both iron and manganese in response to environmental conditions. We used three-electrode systems with working electrodes fixed at 100 mV (vs. SHE) and 400 mV at 50 cm and 70 cm in the valley floor soil of a headwater watershed. Electrodes fixed at 100 mV to mimic iron oxides and at 400 mV to mimic manganese oxides allowed real-time reduction and oxidation rates to be calculated from temporal variations in the electric current. Electrode measurements were compared to soil porewater chemistry, pCO_2, pO_2, groundwater level, resistivity measurements, and precipitation. The fixed-potential electrodes recorded fluctuations over timescales from minutes to weeks. A consistently negative current was observed at 100 mV (interpreted as oxidation of Fe), while the 400-mV electrode fluctuated between negative and positive currents (Mn oxidation and reduction). When the water table rose above the electrodes, reduction was promoted, but above the water table, rainfall only stimulated oxidation. Precipitation frequency thus drove the multi-day reduction or oxidation events (return interval of 5–10 days). These measurements represent the first direct detections of frequency, period, and amplitude of oxidation and reduction events in unsaturated soils. Fixed-potential electrodes hold promise for accurately exploring the fast-changing biogeochemical impacts of metal redox cycling in soils and represent a significant advance for reactions that have been difficult to quantify.

Keywords Anaerobic respiration · Soil respiration · Critical zone · Mineral weathering · Anaerobic microsites

Responsible Editor: Stephen D. Sebestyen.

C. Hodges (✉)
School of Geosciences, University of Oklahoma, Norman, OK, USA
e-mail: chodges@ou.edu

J. M. Regan
Department of Civil and Environmental Engineering, Pennsylvania State University, University Park, PA, USA

B. Forsythe · S. L. Brantley
Earth and Environmental Systems Institute, Pennsylvania State University, University Park, PA, USA

D. Oakley · S. L. Brantley
Department of Geosciences, Pennsylvania State University, University Park, PA, USA

J. Kaye
Department of Ecosystem Science and Management, Pennsylvania State University, University Park, PA, USA

Introduction

Both iron (Fe) and manganese (Mn) are key to the biogeochemical cycling of carbon, nutrients, and trace elements in soils (Borch et al. 2009; Henderson et al. 2012; Herndon et al. 2017; Ma et al. 2020). When soil oxygen (O_2) concentrations are low, many soil bacteria readily switch to Mn and Fe as alternate terminal electron acceptors for respiration (Lovley and Phillips 1988; Pett-Ridge et al. 2006; DeAngelis et al. 2010). This microbially-mediated reduction mobilizes sorbed and coprecipitated carbon, nutrients, and trace metals to porewaters for uptake or leaching to groundwaters (Chacon et al. 2006; Buettner et al. 2014; Linkhorst et al. 2016). As soil pores reoxygenate, the oxidation of both Fe and Mn may generate reactive intermediaries that serve an important role in the decomposition of large organic molecules like lignin (Hall and Silver 2015; Jones et al. 2018).

Despite the importance of these metal redox reactions in soils, they are difficult to measure in situ and the lack of field measurements limits our understanding of the impacts of Fe and Mn redox state changes on soil biogeochemistry. As of now, scientists use a range of active or passive methods to track redox conditions in soils (Fiedler et al. 2007; Scott et al. 2021). Direct measurement of redox potential (Eh) in soils with platinum tip electrodes is useful, but costly. Additionally, measurements of redox potential by platinum electrodes are negatively impacted by micro-scale heterogeneity, and do not provide data on specific redox reactions and rates (Rabenhorst et al. 2009). To address some of the drawbacks of Eh probes, others use passive redox probes of either Fe (Caell and Anderson 1986; Bridgham et al. 1991; Castenson and Rabenhorst 2006; Rabenhorst and Burch 2006; Owens et al. 2008; Hodges et al. 2018) or Mn (Dorau and Mansfeldt 2015, 2016; Scott et al. 2021) to track the presence/absence of reducing or oxidizing conditions relative to a specific redox couple over a set time period. Though they are inexpensive and simple to use, these probes only provide an integrated measure of oxidizing and reducing conditions over the weeks they are installed in the ground. Electrodes with redox-couple specificity and real-time quantification of electron flux would allow for more complete exploration of the frequency and periodicity of metal redox oscillations and therefore the biogeochemical importance of metal redox in subsurface environments.

Recently, graphite electrodes fixed at a specific redox potential were used to track in situ anaerobic microbial metabolism in organic permafrost (Friedman et al. 2013) and riparian zones (Friedman et al. 2016). These fixed-potential electrodes can be used for chronoamperometry to measure the current produced at the electrode surface over time. When set at environmentally relevant redox potentials, the recorded currents indicate the real-time rate of electron flow into or out of the working electrode, where negative currents correspond to oxidation and positive currents to reduction at the set potential.

Given the importance of metal redox cycling and the limitations of traditional redox methods in soils, we sought to apply the method explored by Friedman et al. (2013) to track in situ Fe and Mn redox reactions in upland mineral soils—the first deployment of such electrodes in upland settings with lower soil moisture content. Our goal was to establish the efficacy of these electrodes for tracking Fe and Mn redox cycling in upland soils and demonstrate seasonal metal redox cycling in a well-characterized watershed (Hodges et al. 2019a). Based on measurements reported in Hodges et al. (2019a) at the target watershed (Shale Hills), we hypothesized that reduction of metals would be promoted at the site during the late growing season when demand for O_2 is high and soils are warm and wet after rainfall events. We furthermore hypothesized that these reduced metals would remain in small pores and would only oxidize upon exposure to O_2 following leaf-out and drying in the late spring. To test this hypothesis, we installed graphite electrodes fixed at 100 mV (to mimic Fe oxides) and 400 mV (to mimic Mn oxides) at 50 cm and 70 cm belowground in a valley floor soil at the Susquehanna Shale Hills Critical Zone Observatory (SSHCZO; Fiedler et al. 2007). The SSHCZO is ideal for this installation because it is an intensively monitored watershed with well-documented seasonal and intermittent Fe and Mn redox cycling driven by both abiotic and biotic reactions (Herndon et al. 2011, 2014; Yesavage et al. 2012; Kraepiel et al. 2015; Hodges et al. 2019a). We also monitored soil partial pressure of carbon dioxide (pCO_2), partial pressure of oxygen (pO_2), groundwater level, and porewater chemistry and used these corresponding data to

interpret the currents we measured with the fixed-potential electrodes.

Materials and methods

Susquehanna shale hills site description

Measurements were focused at the south planar valley floor (SPVF; 40.66682° N, 77.9018° W) hillslope position in the Shale Hills catchment of the SSHCZO (Brantley et al. 2013a, b, c, d, 2016, 2017). While named 'valley floor,' to be consistent with past CZO nomenclature, SPVF is at a footslope position. Shale Hills is an intensively monitored, 7.9 ha watershed in the Valley and Ridge physiographic province of central Pennsylvania, USA. The catchment is underlain by the iron-rich Rose Hill shale of the Silurian Clinton Formation, characterized by steep, planar slopes that drain to an intermittent stream that flows from winter through mid-summer (Brantley et al. 2017). This intermittent stream is adjacent to SPVF, and SPVF is monitored with nested lysimeters at 40 and 60 cm, a groundwater monitoring well, and soil gas collection wells at 20, 40, and 120 cm (Fig. 1).

The SPVF soil is an Ultisol where the depth of paralithic contact is 120 cm. The soil is seasonally saturated at the end of winter (Lin et al. 2006). In a fine-scale soil survey of SSHCZO, Lin et al. (2006) mapped SPVF as a moderately well-drained Ernest Series according to the USDA Soil Taxonomy. The Ernest Series is a fine-loamy, mixed, superactive, mesic Aquic Fragiudult. Upslope of SPVF the soils become shallow and well-drained Inceptisols of the Berks and Wiekert series that sit atop fractured shale. Previous work indicates a shallow transient water table that allows preferential flow of soil porewaters downslope over and through this fractured and weathered shale to the valley floor. At SPVF, the porewaters from upslope mix with older, deeper groundwaters beneath the valley floor (Lin et al. 2006; Jin et al. 2011).

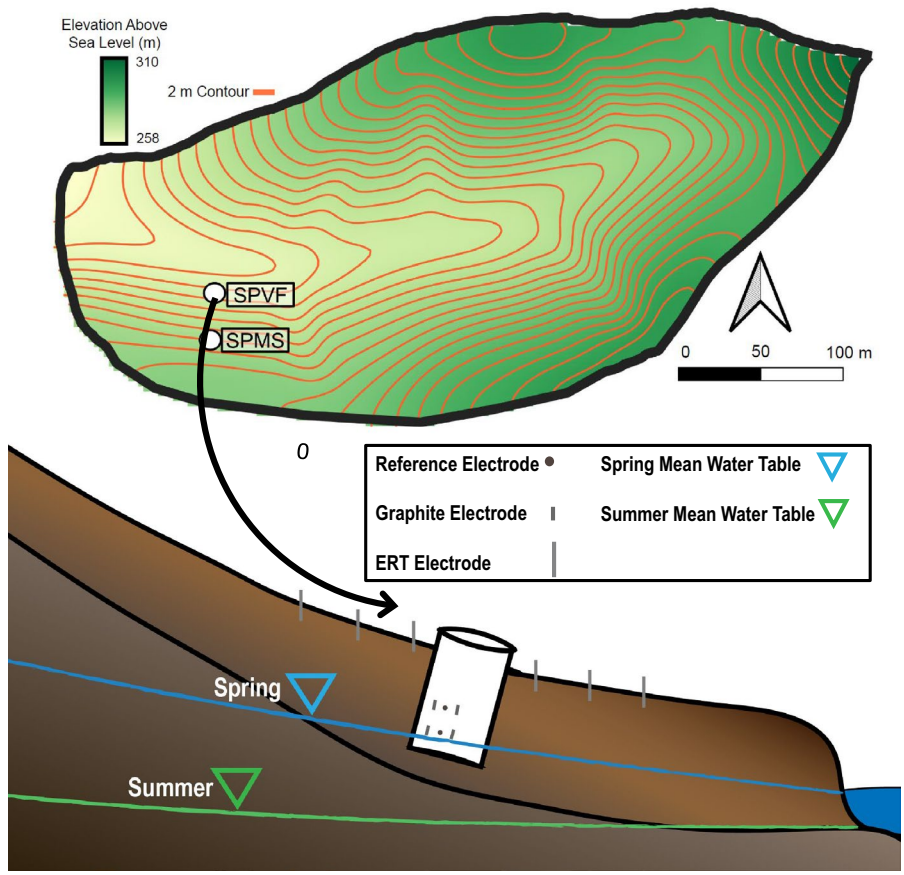

Fig. 1 *Upper* Map of the Shale Hills Watershed. *Lower* Diagram of the electrode installation at the south planar valley floor (SPVF) site. Elevation above sea level is indicated by color gradient in the upper figure, with lighter green denoting lower elevation and darker green denoting higher elevation. Orange lines indicate the two-meter contour lines. White circles demonstrate the location of SPVF and south planar midslope (SPMS). In the lower diagram, blue and green lines represent the perched water table depth at the beginning (spring) and end (summer) of the growing season. The black line represents the augerable soil depth

Fixed potential electrode installation and analysis

We installed graphite-based three-electrode systems at 50 and 70 cm in the soil at SPVF in March 2019. We chose those depths at SPVF because there are contrasting soil properties and soil moisture conditions that we anticipated would lead to different redox conditions over the growing season. The depth of the perched, seasonal high-water table at this position is about 70 cm below the land surface. The 50-cm electrodes are in a Bw horizon characterized by silty clay loam soil texture and no redoximorphic features. The 70-cm electrodes were installed in the Bt horizon, which is characterized by a silty clay texture and redoximorphic Fe concentrations and depletions. The soil pH was reported in that location as 4.7 at 50 cm and 5.0 at 70 cm (Jin et al. 2010). Additionally, porewater pH monitored between 2006 and 2011 in about 50 samples from SPVF yielded an average pH of 4.9 ± 0.1 standard error at 40 cm and 4.8 ± 0.1 standard error at 60 cm (Brantley et al. 2013a, b, c; Herndon et al. 2015).

In May 2019 we additionally installed three-electrode systems at 20 cm and 50 cm at the south planar midslope (SPMS) above SPVF to collect additional data in an oxic site for comparison. However, that site was abandoned because the soil conditions caused desiccation of the reference electrodes and loss of contact of the working electrodes with the soil. The subsurface soils at SPMS are very channery to extremely channery, and the presence of these channers (flat pieces of shale) prevented full electrode contact with the soil, and therefore desiccation. Desiccation was recognized by crystallization of the AgCl reference solution around the tip of the reference electrode. Other well-drained soils with fewer coarse fragments would possibly not have the same limitations.

The three-electrode system installed at both depths of SPVF consisted of a graphite plate working electrode ($10 \times 2.5 \times 0.6$ cm dimensions), a graphite counter electrode identical to the working electrode, and a reference electrode. Each electrode component was emplaced in contact with the soil. Since redox mediator addition is not feasible in a subsurface field deployment for these electrochemical techniques, direct contact between the soil and the electrodes improves the likelihood of redox equilibria between redox-active minerals and the working electrode (Sander et al. 2015). The glass Ag/AgCl reference electrode provides the benchmark for the potential imposed on the potentiostatically maintained working electrode. The current was then measured between the working electrode and counter electrode in each three-electrode bundle. Negative currents represent oxidation at the set potential, that is, electron flow out of the electrode. Positive currents represent reduction, that is electron flow into the electrode at the set potential.

To install the electrodes, a hole was dug to match the diameter (40 cm) of a schedule 80 polyvinyl chloride (PVC) pipe. Slots were cut in the PVC pipe at 50 and 70 cm below the soil surface so that the working, reference, and counter electrodes could be pushed through the slots and into the soil. Slots for the reference electrodes were positioned within 1 cm of the working electrodes, and counter electrodes were spaced about 4 cm from the associated working electrode. The three electrodes were inserted into their respective slot and pushed into the soil until only approximately 3 cm remained extended inside the pipe. Graphite working and counter electrodes were installed so that the thinnest dimension was parallel to the soil surface, to prevent the potential for water ponding atop the electrodes.

Once installed, the pipes were capped and sealed to prevent atmospheric air and precipitation from entering but remained open at the bottom contact with the soil. Surface soil was mounded around the tubes to prevent formation of preferential flowpaths around the PVC. The capped tops allowed for access to working and counter electrodes for refurbishment and replacement of reference electrodes. The Ag/AgCl reference electrodes were checked monthly and replaced as needed when reference solution showed crystallization or no longer remained in the glass body of the electrode.

Potentials at the graphite working electrodes were poised using Nanoelectra Nev4 USB potentiostats (Nanoelectra S.L. Madrid, Spain) connected to a field laptop (Latitude 5430 Rugged PC, Dell, Round Rock, Texas, USA), with current data collected every 30 s and stored on the laptops. For analysis and data visualization, currents recorded by the potentiostats were averaged every 12 min. Potentials were set at 100 mV relative to the standard hydrogen electrode (SHE) to mimic the redox potential of Fe oxides (Fiedler et al. 2007). To complement the 100 mV data, a second set

of electrodes were installed in an adjacent pipe at 50 and 70 cm at SPVF in late April 2020 and fixed at 400 mV vs. SHE. This redox potential was chosen to bracket the range of suboxic redox potentials in soil, and mimic the redox potential of Mn oxides in soils (Fiedler et al. 2007). The specific redox potential at which species are reduced is dictated by factors that include pH, the activity of the species in solution, the ionic strength, and the identity of the oxidant (Stumm and Morgan 1996), and all of these can vary in natural systems. Therefore, both Mn and Fe are redox-active across a range of potentials rather than just one potential. We chose the 100 and 400 mV redox potentials as points at which Fe or Mn are likely to be reduced, respectively, given soil and solution pH values around 5 (Stumm and Morgan 1996).

From the measured currents, we calculated the oxidation and reduction rates at 100 mV (in 2019 and 2020) and 400 mV (in 2020 only). For the electrodes at 100 mV, we calculated the rate of the redox reactions in terms of Fe reduced or oxidized, for example, as written in Eq. 1.

$$Fe_2O_3 + 2e^- + 6H^+ \longleftrightarrow 2Fe^{2+} + 3H_2O \quad (1)$$

At 400 mV, we calculated the rate of the redox reactions in terms of Mn reduced or oxidized (Eq. 2).

$$MnO_2 + 2e^- + 4H^+ \longleftrightarrow Mn^{2+} + 2H_2O \quad (2)$$

Equations 1 and 2 represent reactions with example minerals (hematite and pyrolusite, respectively), but the fixed-potential electrodes are likely to allow electron (e^-) transfer into many Fe and Mn (oxy)hydroxides, including ferrihydrite, goethite, and birnessite (Friedman et al. 2013; Logan et al. 2019). It is also possible that electron transfer occurs into amorphous metal oxides, Fe- or Mn-containing silicates, or organic matter (Roden et al. 2010; Shelobolina et al. 2012). We nonetheless assume for our rate calculations that e^- transfer occurs only with Fe or Mn minerals, and that there is full oxidation or reduction of Mn (i.e., no accumulation of Mn^{3+}). This is a necessary and reasonable assumption to interpret the current measurements. We also assume low concentrations of other more thermodynamically favorable terminal electron acceptors such as NO_3^-, as previous studies at the site have demonstrated that NO_3^- concentration in porewaters rarely exceeds 0.15 ppm NO_3^--N (Weitzman et al. 2018).

The extent of metal reduction was calculated based on the integrated value of all positive currents at the corresponding working electrode potential (I_{red}) over the monitoring period (t_0 to t_f), which were then divided by Faraday's constant (F) to convert to moles of electrons transferred. Using the assumed reaction stoichiometries (Eqs. 1, 2), the surface area of the electrodes in contact with the soil (*SA,* about 30 cm^2 in contact with the soil), and an estimate of the specific surface area (*SSA,* 25 $m^2\ kg^{-1}$) of the bulk soil (Jin et al. 2010a) attributable to oxides of Fe (SSA_{Fe}, 1% of *SSA* at 50 cm, 1.2% at 70 cm; Yesavage et al. 2012) or Mn (SSA_{Mn}, 0.1% of *SSA* at 50 and 70 cm; Herndon et al. 2011; Kraepiel et al. 2015) at SPVF, we calculated the extent of Fe or Mn reduced (Fe_{red} or Mn_{red} in mol $g.^{-1}$ soil) over the monitoring period in each season (Eqs. 3, 4)

$$Fe_{red} = \frac{\int_{t_0}^{t_f} I_{red} dt}{F \times SA} SSA_{Fe} \quad (3)$$

$$Mn_{red} = \frac{\int_{t_0}^{t_f} I_{red} dt}{2F \times SA} SSA_{Mn} \quad (4)$$

Oxidation extent (Fe_{ox} or Mn_{ox} in mol g^{-1} soil) was calculated similarly, but was based upon the integrated value of all negative currents at the corresponding working electrode potential (I_{ox}) over the monitoring period (Eqs. 5, 6).

$$Fe_{ox} = \frac{\int_{t_0}^{t_f} I_{ox} dt}{F \times SA} SSA_{Fe} \quad (5)$$

$$Mn_{ox} = \frac{\int_{t_0}^{t_f} I_{ox} dt}{2F \times SA} SSA_{Mn} \quad (6)$$

We also calculated average rates of Mn and Fe oxidation and reduction per mass of soil ($\overline{r_{ox}}, \overline{r_{red}}, \mathrm{mol}\ g^{-1}\ d^{-1}$). For each monitoring period, we calculated the average positive or negative currents and replaced the integrated current in Eqs. 3 through 6 with the calculated average (Eq. 7 shows average Fe reduction rate).

$$\overline{r_{Fe,red}} = \frac{\overline{I_{Fe,red}}}{F \times SA} SSA_{Fe} \quad (7)$$

In this first effort to show efficacy of the electrodes in unsaturated soils, we made no attempt to define the

specific redox chemistry in the system. Therefore, these calculations allow use of the measured currents to determine an "apparent" electron transfer with respect to Fe or Mn at the set potentials. We acknowledge that other species are likely present in the soil system and contributing to exchange of electrons at the redox potentials of 100 mV and 400 mV. Therefore, the values calculated from Eqs. 3–7 are considered maximum estimates of Fe or Mn oxidation or reduction at the set potentials.

Concurrent data collection

Soil porewater, pCO_2, pO_2, precipitation, groundwater level, and volumetric soil water content were monitored to correspond with the fixed-potential electrode measurements made at SPVF. The soil porewaters at SPVF were collected with suction lysimeters at 40 cm and 60 cm. These lysimeters were installed for previous projects (e.g., Jin et al. 2010) and therefore the depths of sampling are not the same as the depth of electrode installation. Tensions of − 50 kPa were set at the lysimeters and porewaters were collected 1 h afterward to limit the exposure of reduced Fe to atmospheric O_2. All lysimeters were still sealed under vacuum at the 1 h sampling point. While O_2 from within soil may have interacted with collected porewaters, the vacuum and short time for samples to draw was intended to limit the potential for oxidation of reduced Fe in porewaters. Samples were immediately acidified to a pH of two with hydrochloric acid to preserve the oxidation state of Fe in solution (Stumm and Morgan 1996). All porewater samples were subsequently refrigerated within four hours of collection prior to analysis.

Porewaters were measured specifically for dissolved Fe^{+2} and Fe^{tot} determination with the ferrozine assay (e.g., Viollier et al. 2000; Huang and Hall 2017). We used hydroxylamine hydrochloride to reduce all Fe in solution prior to the ferrozine assay to measure Fe^{tot}. Absorbances were measured with a UV–Vis spectrophotometer (Biotek, ELx808 absorbance reader, Agilent, Santa Clara, California, USA). The detection limit of this method is 0.05 ppm Fe. Samples were run in triplicate and concentration measurements were accepted if coefficient of variation was less than 5%.

Soil moisture sensors (Stephens HydraProbe, Stephens Water Monitoring Systems, Oregon, USA), again installed at SPVF for a different study (Jin et al. 2011), recorded volumetric water content every 15 min at 20 cm and 40 cm. Data were recorded by a datalogger (CR1000X, Campbell Scientific, Logan, Utah, USA). Datalogger malfunction during 2020 caused a loss of soil moisture data during the monitoring period, and so only 2019 data are presented here. Groundwater level was monitored at a well adjacent to SPVF. The well was installed in 2009 by power auger to a depth of 4 m below the land surface and is slotted in the last 1 m. Groundwater level in the well was recorded every 15 min using a HOBO U20-001-01 non-vented pressure transducer (Onset Computer Corporation, Bourne, Massachusetts, USA). Precipitation and air temperature were also monitored at the site using an OTT Pluvio^2 weighing rain gauge (OTT Hydromet, Kempten, Germany) and a Campbell Scientific HMP45C temperature and relative humidity probe. Precipitation and air temperature were recorded every 10 min, again with a Campbell Scientific CR1000X datalogger.

In 2019 soil pCO_2 and pO_2 were monitored at the soil gas wells at SPVF. Hasenmueller et al. (2015) summarized the installation procedure for the soil gas wells and Hodges et al. (2019a) outlined the analysis procedure for pCO_2 and pO_2 data. Samplers were constructed of stainless-steel tubing with stainless-steel mesh affixed to one end. Holes were augered to the desired depth—in this case 20, 40, and 120 cm—and the samplers were placed in the hole. Sieved coarse fragments from the soil were installed around the mesh end to prevent the gas tube from filling with soil and then sieved < 2 mm soil was used to backfill the holes to limit the potential for vertical air movement. We include the 120-cm soil gas data as an indicator of conditions in the soil horizon below the one in which the 70-cm electrodes are installed.

While sampling was attempted every 2 weeks, high soil moisture at times in May 2019 limited sampling because the tubes were filled with water. Airtight syringes with a one-way lock were used to sample the gas tubes for pCO_2. All gas tubes were purged of 5 mL of gas in the 20- and 40-cm wells, and 10 mL of gas in all 120-cm wells to ensure sampling of soil atmosphere, and not dead air in the tube. Immediately after purging, 5 mL of soil gas were collected with the locking syringe for analysis in the laboratory. Afterward, 10 mL of soil gas were sampled for pO_2 using a handheld soil gas analyzer (model 901,

Quantek Instruments, Grafton, Massachusetts, USA). The Quantek 901 has a range of 0 to 100% O_2 and an accuracy of ± 0.1% O_2. As recommended by the manufacturer, the Quantek is calibrated using O_2-free gas and ambient air every four years. Three samples of ambient air were collected with locking syringes 30 cm above the ground surface per hillslope position for ambient CO_2. Soil gas samples were analyzed in the laboratory on a flow-through infrared gas analyzer (LI-7000, LiCOR Inc.) within two days of collection. Measurement accuracy is within 1% of measured value.

The 2019 pCO_2 and pO_2 samples were assessed based on the 1:− 1 molar relationship expected for aerobic carbohydrate respiration, corrected for gas diffusion as detailed in Angert et al. (2015) and Kim et al. (2017). Results are presented in this paper in the same way as previous publications reporting results from the SSHCZO (Hodges et al. 2019a, 2021). Briefly, the soil gas data are plotted as pCO_2 vs. pO_2, relative to a line defined by a slope of −0.76 (the ratio of the two diffusion constants) and an x-axis origin of 20.95% (the concentration of O_2 in the atmosphere). When data deviate from this line, processes other than aerobic respiration of carbohydrates and gas diffusion are affecting soil pCO_2 or pO_2 (Hodges et al. 2019a, 2021). In this study, data falling above the theoretical line indicate excess CO_2 in the soil pore gas compared to changes in O_2, and are thus interpreted to document contributions to soil gas from anaerobic respiration. Based on previous interpretations for Shale Hills and nearby areas (Hodges et al. 2019a, 2021), and prior work (Angert et al. 2015), points below the theoretical line indicate greater O_2 depletion relative to CO_2 in the soil atmosphere than predicted by aerobic carbohydrate respiration stoichiometry. Here these gas ratios are interpreted as showing the possibility of chemolithoautotrophic or abiotic oxidation.

Because the gas wells at SPVF were often flooded in the sampling period of 2019, we installed soil CO_2 and O_2 sensors at 50 and 70 cm at SPVF in March of 2020. Sensors can measure soil gas even under high soil moisture conditions and these depths provide clear insights into the biotic and abiotic processes affecting soil CO_2 and O_2 at the depths of our fixed-potential electrode measurements. Unfortunately, the O_2 sensors failed two months after installation, and were not fixed because of issues related to the Covid-19 pandemic. Therefore, we report only pCO_2 data collected in 2020. Soil pCO_2 at 50 and 70 cm in SPVF was sensed by an optical electrode (Eosense, EosGP, Dartmouth, Nova Scotia, Canada), and was recorded every 15 min. Data were recorded by a datalogger (CR1000X, Campbell Scientific, Logan, Utah, USA).

Electrical resistivity tomography

Interpreting metal redox cycling in upland soils requires understanding the soil moisture regime. To map changes in soil moisture weekly from mid-May through the end of June 2020, we used time lapse 3-D electrical resistivity tomography (3D ERT). An Iris Instruments (Orleans, France) Syscal Pro sounding resistivity meter was used to record resistivity. Resistivity electrodes were arrayed in a rectangle centered around the fixed-potential electrodes at an interval spacing of 1.5 m with 8 resistivity electrodes in the x direction (parallel to stream) and 6 in the y direction (Fig. 1; perpendicular to the stream, going upslope). Data were imported into the Iris Instruments Prosys II software where missing data and anomalously high data points were removed. Res3D-Inv (Aarhus GeoSoftware, Aarhus Denmark) was used to create inversions of resistivity datasets. These inversions provide 3-dimensional visualizations of estimated resistivity at each measurement date. Since soil texture and structure were assumed to remain constant over the sampling period, any change in resistivity corresponds with a change in soil moisture conditions. Higher resistivity indicates relatively drier conditions and lower resistivity indicates relatively wetter conditions (Michot et al. 2003; Samouëlian et al. 2005; Garré et al. 2011).

Data analysis

Unless otherwise noted (e.g., 3D ERT datasets), all analyses, calculations, and data visualizations were performed using Python (Gosset and Wright 2017). The pandas package (McKinney 2010; Pandas Development Team 2020) was used for data management, analysis, and quality assurance. Data visualization was performed using the matplotlib (Hunter 2007) and seaborn packages (Waskom 2021). The SciPy package was used for the calculation of rates and extents of redox reactions (Virtanen et al. 2020).

Results

Fixed-potential electrode measurements

The fixed-potential electrodes in 2019 and 2020 indicated periodic redox fluctuations at 100 and 400 mV in the subsurface of SPVF (Figs. 2 and 3). In the Spring of 2019, data were collected in the two-month period between April and June. At 50 cm, negative currents (to about − 0.3 mA) were detected periodically, but otherwise currents remained negligible (Fig. 2). The longest non-zero event at 50 cm in Spring 2019 lasted for about 3 days. Negative currents represent movement of electrons out of the electrodes (i.e., cathodic electrode response) into the soil. We thus infer these results as oxidation Fe^{+2} in

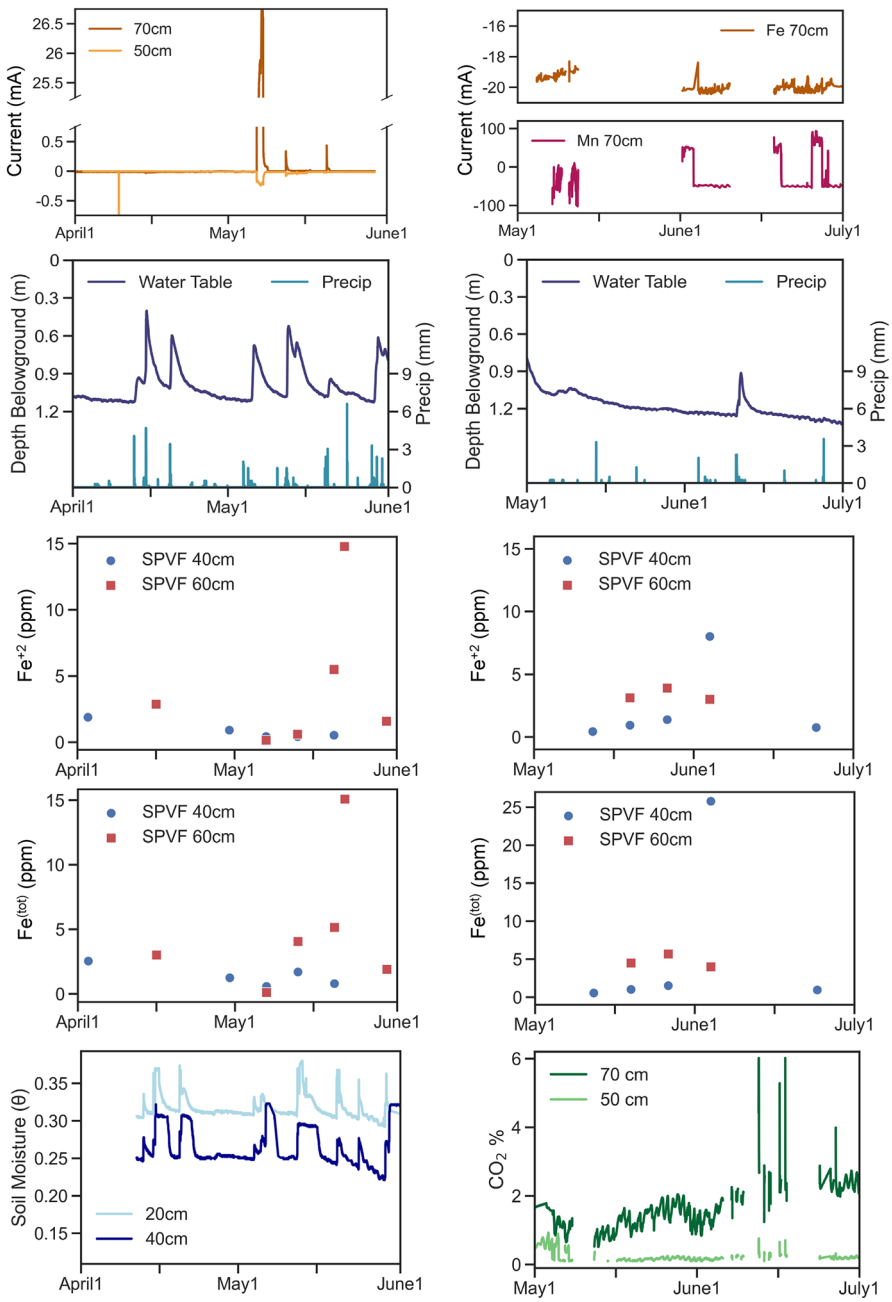

Fig. 2 Measurements over the early growing season in 2019 (left) and 2020 (right). From top to bottom, the left panels represent measured currents at the 50-cm and 70-cm 100 mV electrodes at SPVF, water table level (m) and 10-min precipitation (mm), Fe^{2+} concentrations in porewaters (ppm), total Fe concentration in porewaters (ppm), and volumetric water content at 20 cm and 40 cm. From top to bottom the right panels represent measured currents at the 70-cm 100 and 400 mV electrodes, water table level (m) and 10-min precipitation (mm), Fe^{2+} concentrations in porewaters (ppm), total Fe concentration in porewaters (ppm), and sensor-measured CO_2 concentrations at 50 and 70 cm

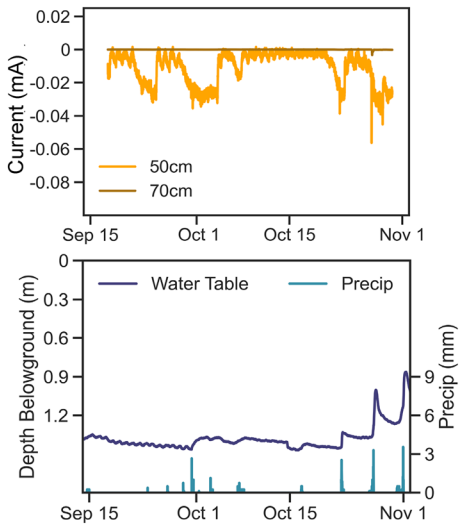

Fig. 3 Data collected over the late growing season in 2019. The top panel represents measured currents at the 50-cm and 70-cm 100 mV electrodes, and the bottom panel represents water table level and 10-min precipitation. Soils were too dry to produce porewater samples for Fe analysis

the soil at 100 mV. At 70 cm, currents were at 0 mA or periodically became positive and reached a maximum of about 26.5 mA (Fig. 2). There were three such reducing events at 70 cm that lasted from one to three days, separated by about three to five days in May 2019. Positive currents represent a movement of electrons out of the soil and into the electrode (i.e., anodic response) and thus represent reduction of soil Fe oxides at 100 mV. The periodic negative currents at 50 cm and positive currents at 70 cm co-occurred over the 2-month sampling period (Fig. 2).

In 2019, currents were measured, and data were also collected between September 15 and November 1. At 70 cm, currents remained at 0 mA throughout the monitoring period. At 50 cm, currents oscillate near 0 but occasionally were recorded equal to about − 0.4 mA for periods of about 2–5 days (Fig. 3).

In 2020, currents were measured, and data were collected in a 2-month period between May and July (Fig. 2). Here, we only show the data from the 70-cm electrodes, as currents measured at 50 cm at each fixed potential remained around 0 mA throughout the sampling period. In 2020, currents measured at the electrode fixed at 100 mV remained around − 20 mA throughout the sampling period. On the other hand, currents measured at the electrode fixed at 400 mV revealed variations between negative and positive currents from a low of around − 100 mA in mid-May to a peak around 100 mA near the end of June (Fig. 2).

From the fixed-potential electrode measurements in 2019 and 2020, we calculated the average oxidation and reduction rates ($\overline{r_{ox}}$, $\overline{r_{red}}$) and the extent of oxidation/reduction ($Mn_{ox/red}$ and $Fe_{ox/red}$) at 100 and 400 mV during the monitoring periods (Table 1). In spring 2019, non-zero currents at the 50-cm electrodes correspond to *Fe* $\overline{r_{ox}}$ of 1.9 mmol g^{-1} d^{-1} and an *Fe* $\overline{r_{red}}$ of 0 mmol g^{-1} day^{-1}. At 70 cm in spring 2019 *Fe* $\overline{r_{ox}}$ was 1.4 mmol g^{-1} d^{-1} and an *Fe* $\overline{r_{red}}$ of 108 mmol g^{-1} day^{-1}. Activity at the electrodes correspond to an Fe_{ox} of 0.98 mmol Fe kg^{-1} and an Fe_{red} of 0 mmol Fe kg^{-1} at 50 cm, and Fe_{red} of 39 mmol Fe kg^{-1} and an Fe_{ox} of 0.67 mmol Fe kg^{-1} at 70 cm. The average rates and extents of Fe reduction or oxidation

Table 1 Rate and extent of oxidation and reduction at the fixed potentials

	Average metal oxidation rate	Average metal reduction rate	Extent of metal oxidized	Extent of metal reduced
	mmol metal g^{-1} d^{-1}		mmol metal kg^{-1} soil	
Spring 2019				
100 mV, 50 cm	1.9	0	0.98	0
100 mV, 70 cm	1.4	108	0.67	39
Fall 2019				
100 mV, 50 cm	1.3	0	0.58	0
Spring 2020				
100 mV, 70 cm	2000	0	750	0
400 mV, 70 cm	0.19	0.15	15	34

account for the 2-month monitoring period at the beginning of the 2019 growing season.

In Fall 2019, currents at the 70-cm electrode remained around 0 mA throughout the monitoring period, but there were oxidizing events at 50 cm (Fig. 3). Over this sampling period the measured currents correspond to an $Fe\ \overline{r_{ox}}$ of 1.3 mmol g^{-1} day^{-1} and an Fe_{ox} of 0.58 mmol Fe kg^{-1}.

In 2020, we observed no activity at the sensors at 50 cm, but a strong signal of oxidation at 100 mV and oscillations between oxidation and reduction at 400 mV. Also, in comparison to 2019, the detected currents in 2020 were of a greater magnitude. Non-zero currents at the 100 mV 70-cm electrodes correspond to $Fe\ \overline{r_{ox}}$ of 2 mol g^{-1} day^{-1} and an Fe_{ox} of 0.75 mol Fe kg^{-1}. At the 400 mV electrodes, $Mn\ \overline{r_{ox}}$ was 0.19 mmol g^{-1} day^{-1} and an $Mn\ \overline{r_{red}}$ of 0.15 mmol g^{-1} day^{-1}. Activity at these electrodes correspond to Mn_{red} of 34 mmol Mn kg^{-1} and Mn_{ox} of 15 mmol Mn kg^{-1} soil.

Water table, soil moisture, and precipitation

In general, soils were wetter in Spring 2019 than in Spring 2020 (Fig. 2), while average air temperatures, which increased from around 8 °C in April to 22 °C in July, were about the same in 2019 and 2020. In 2019 precipitation events were frequent between April and June with a total of about 23 cm of rain falling in the 61-day period. This precipitation caused fluctuations in the perched water table up to and above the sensors installed at 50 and 70 cm. In Fall 2019, about 15 cm of rain fell in the 65-day period. The perched water table rose after precipitation events and to a minimum of 90 cm below the land surface by the end of the monitoring period (Fig. 2). From May through June 2020, precipitation was infrequent, resulting in half the volume of precipitation as observed in Spring 2019 (10 cm). This infrequency of precipitation caused the water table to remain below 100 cm through most of the 2-month period (Fig. 2).

Porewater chemistry

We measured the concentration of Fe^{2+} and Fe^{tot} ($Fe^{2+} + Fe^{3+}$) in porewaters at 40 cm and 60 cm at SPVF over the sampling periods in 2019 and 2020. In general, concentrations of Fe^{2+} and Fe^{tot} remained below 5 ppm throughout both the 2019 and 2020 growing seasons (Fig. 2).

In 2019, we measured a maximum of 15 ppm Fe^{2+} at the 60-cm SPVF lysimeter, while porewater Fe concentrations remained below 3 ppm at 40 cm. Additionally at both 40 and 60 cm in SPVF, Fe^{2+} and Fe^{tot} were about the same concentration in each sample. Because Fe^{tot} is a combined measure of Fe^{2+} and Fe^{3+}, the lack of difference in concentration between Fe^{2+} and Fe^{tot} indicates that most dissolved Fe was Fe^{2+}.

Porewaters collected in 2020 indicated low Fe concentrations (< 5 ppm) at both SPVF throughout much of the sampling period (Fig. 2). The maximum recorded Fe^{2+} and Fe^{tot} concentrations of about 8 ppm Fe^{2+} and 25 ppm Fe^{tot} were collected from the 40-cm SPVF lysimeter at the beginning of June. All other samples collected did not show such a difference between concentrations Fe^{+2} and Fe^{tot}, indicating that most Fe in solution was reduced.

Soil gases

In 2019, soil pCO_2 and pO_2 were hand-sampled between April and June. Sampling was attempted at 20, 40, and 120 cm, but few samples were obtained from 120 cm due to inundated gas wells. The soil-gas measurements were consistent with the stoichiometry of aerobic respiration perturbed by diffusion (Angert et al. 2015) as discussed in Methods. These two processes were inferred to be the prevailing controls on the two gases because the data mostly plot along the line representing aerobic respiration and diffusion (Fig. 4). However, there are some points, most notably sampled from 20 and 40 cm, that fall well-below the line representing the stoichiometry between pCO_2 and pO_2 expected when aerobic respiration and gas diffusion are the dominant processes.

In 2020, soil pCO_2 was sensed and recorded at 15-min intervals from the beginning of May through mid-July at 50 and 70 cm, the depths of the fixed-potential electrodes (Fig. 2). Throughout the monitoring period, soil pCO_2 was higher at 70 cm than at 50 cm. At 70 cm soil pCO_2 was lowest at the beginning of May, around 1%, and increased to vary around 2% in July. There were additional periodical peaks, some to above 6%, at 70 cm. Contrasting with 70 cm, 50 cm soil pCO_2 was highest around the beginning of

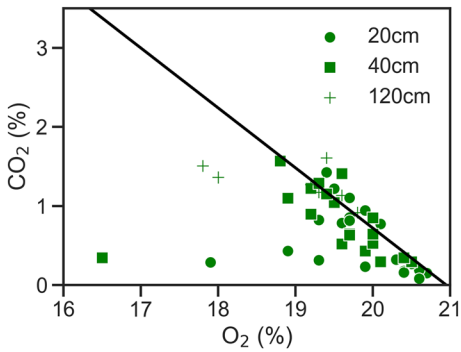

Fig. 4 Soil pCO_2 and pO_2 measured at SPVF from 20-cm, 40-cm, and 120-cm gas wells in 2019. Different symbols represent data from different soil depths. The black line represents the theoretical relationship of soil pCO_2 vs. pO_2 given aerobic respiration on a carbohydrate substrate and gas diffusion

May and remained below 1% throughout the rest of the monitoring period.

Soil 3D ERT in 2020

From May 20 through June 24 in 2020 we used weekly 3D ERT measurements to track the change in soil moisture conditions around the fixed-potential electrodes. We present inversions (i.e., estimates of subsurface resistivity) of the apparent resistivity measurements along both the X–Y and X–Z axes. When examining resistivity along the X–Y axis such that each slice represents conditions at a single depth, it is clear that resistivity was higher, and therefore soil moisture was lower, at 50 cm than it was at 70 cm (Fig. 5). In the panels of Fig. 5, the 100 mV electrodes are located at x = 2.5 m, y = 1.5 m, and the 400 mV electrodes at x = 1.25 m, y = 1.5 m. At 50 cm, the resistivity around the electrodes was above 250 Ω*m for most of the 6-wk monitoring period. At 70 cm resistivity was consistently lower, around 150 Ω*m. Although differences in depth are apparent over these dates, there was not much change in resistivity over the 6 weeks.

This lack of change in resistivity (and therefore soil moisture) over time from May 20, 2020 through June 24, 2020 is clear when examining slices along the X–Z axis located at the point along the y axis where the electrodes were installed (Fig. 6). In these slices, the 400 mV electrodes are located at x = 1.25, z = 50, 70; and the 100 mV electrodes are located at x = 2.5, z = 50, 70. In addition to the lack of change in resistivity over time in these soils, it also appears that there was a zone of higher resistivity centered around the area that the 100 mV electrodes are installed compared to the 400 mV electrodes.

Discussion

These data show, for the first time, the in situ dynamics of metal redox in upland mineral soils. Though this was a proof-of-concept study that did not emphasize replication or chemical analysis of redox processes, we discovered that the fixed-potential electrodes can be used to observe the rate, amplitude,

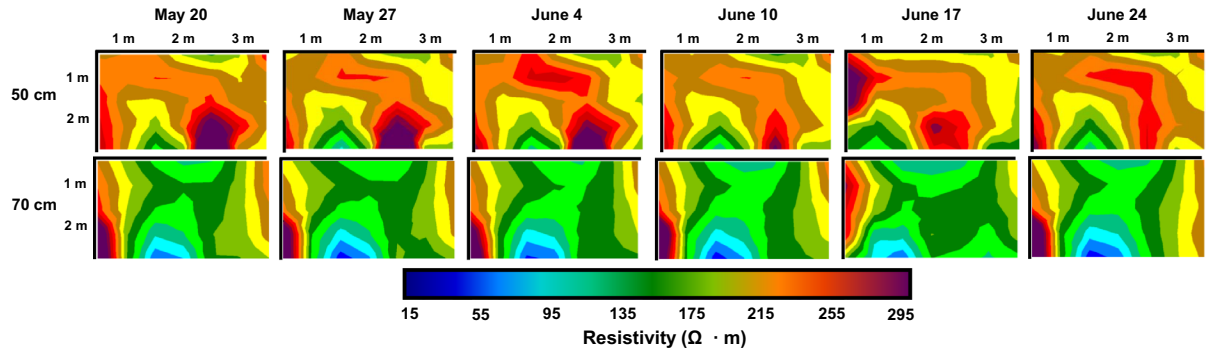

Fig. 5 Soil ERT slices along the X–Y axis from the weekly measurements in 2020. These slices represent the change of resistivity at a single depth over time centered around the fixed-potential electrodes. The top row represents resistivity at 50 cm, and the bottom row resistivity at 70 cm. The bottom of each plot is towards the stream, and the top of each plot is oriented upslope. Warm colors represent higher resistivity and therefore dryer conditions, cool colors represent lower resistivity and wetter conditions

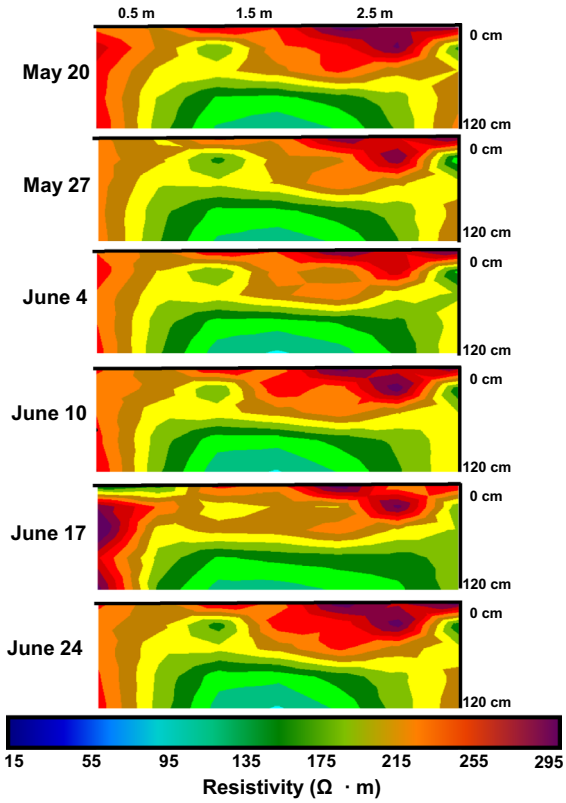

Fig. 6 Soil ERT slices along the X–Z axis from the weekly measurements in 2020. These slices represent the change of resistivity with depth in the soil profile and over time centered around the fixed-potential electrodes. The 400 mV electrodes are installed at 1 m and the 100 mV at 2.5 m along the X axis. Warm colors represent higher resistivity and therefore dryer conditions, cool colors represent lower resistivity and wetter conditions

period, and frequency of redox events in the early and late growing season of an upland soil. In the next sections we discuss the redox dynamics observed at SPVF, the spatial heterogeneity of those redox reactions elucidated from the 3D ERT measurements, the apparent controls of soil moisture on metal redox at Shale Hills, and the significance of our work in the context of the roles that metal oxides play in the biogeochemical functioning of upland soils.

Fixed-potential electrodes reveal in situ redox dynamics

The results from SPVF show redox fluctuations between negative and positive currents for both potentials of 100 mV and 400 mV. From these data we infer that both Fe and Mn are actively redox cycling. The only known previous installations of fixed-potential electrodes documented smaller magnitude positive currents in thawing permafrost soils where Fe reduction is known to account for over half of soil respiration (Lipson et al. 2010; Friedman et al. 2012, 2013), or in riparian zones with active methanogen populations (Friedman et al. 2016). Our results show that fixed-potential electrodes are useful for documenting not only reduction dynamics but also oxidation dynamics and can be used in moderately well-drained upland soils. Our results and those reported by Friedman et al. (2012, 2013, 2016) therefore show that fixed-potential electrodes can be used to measure redox-generated currents in many soils (permafrost soils, riparian floodplain soils, and moist upland soils) to document reduction *and* oxidation reactions across a range of redox potentials. However, as our abandoned site at SPMS demonstrates, some soils, particularly those with high fractions of coarse fragments or those that are dry, may pose challenges for electrode placement and maintenance of the reference electrode.

The fixed-potential electrodes generate high temporal-resolution data that elucidate mechanisms and drivers of metal redox cycling in upland soils. For example, in 2019 we measured currents consistent with Fe reduction at 70 cm that corresponded with water table rise after rainfall events. On the other hand, in the Fall of 2019, oxidation events at 50 cm corresponded directly to precipitation events. Oxygen-charged rainwaters likely stimulated oxidation of Fe in previously dry soils as they percolated through SPVF.

In 2020, currents measured at the 70-cm electrodes were consistent with both oxidation and reduction at 400 mV; we interpret these results represent redox cycling of Mn. Over the monitoring period, the reduction at 400 mV was more or less balanced by subsequent oxidation as the current direction and magnitude inverted. In this situation, weekly monitoring of porewater chemistry or measurements of pCO_2 and pO_2 may suggest only aerobic respiration. Such observations point to the value of in situ real time measurements to observe redox fluctuations in soils.

The fixed-potential electrodes indicate high average Fe reduction rates (1.7 mmol Fe g^{-1} day^{-1} at 70 cm in 2019) compared to the limited datasets published from other subsurface soils in upland

temperate watersheds. For example, during the spring in an upland soil in the Piedmont of South Carolina, USA the Fe reduction rate—calculated by change in HCl-extractable Fe^{2+} over a 2 week period—at 60 cm was 0.02 mmol Fe kg^{-1} day^{-1}, orders of magnitude lower than the rate we recorded at SPVF (Hodges et al. 2019b). At the same time, the total extents of reduction at the two sites were similar. This comparison demonstrates that the temporal resolution of our measurements yields insights into Fe redox rates in upland soils that would otherwise be difficult to resolve with other methods. In general, the soils of SPVF are oxidizing most of the time and only become reducing for less than 10% of the monitoring periods. Reduction is stimulated in response to precipitation or water table rises.

Porewater chemistry is consistent with the high Fe reduction rates calculated from the fixed potential electrodes in 2019. While the baseline concentrations of 1 to 2 ppm Fe^{+2} and Fe^{tot} in the soil solution at SPVF are comparable to average conditions in other temperate forests (Fuss et al. 2010; Schaetzl and Rothstein 2016), the peaks in Fe^{+2} around 15 to 25 ppm are more like the measured porewater concentrations of 18 ppm Fe^{tot} in freshwater marsh soils of Virginia, USA (Chambers and Odum 1990) and the 20 ppm Fe^{2+} reported for wetland soils in a headwater catchment in Bavaria (Knorr 2013). The high rate of Fe reduction and the high Fe^{2+} concentrations in porewaters at Shale Hills reflect the acidic soils and high concentration of Fe in the parent material of Shale Hills, but also point to the significance of Fe redox fluctuations to biogeochemical cycling at the site (Jin et al. 2010; Yesavage et al. 2012).

Our findings both substantiate past results and provide novel insights into past work at Shale Hills with respect to Fe and Mn redox cycling. For example, Hodges et al. (2019a), using soil pCO_2 and pO_2 measurements distributed across the Shale Hills watershed, found indirect evidence of seasonal metal redox cycling based on soil gases throughout the watershed, with the most pronounced patterns at SPVF.

With respect to earlier work on Fe redox at Shale Hills, Yesavage et al. (2012) found evidence of Fe reduction and subsequent oxidation through calculations of Fe enrichment and depletion relative to the shale parent material. They also reported the presence of Fe-oxidizing and -reducing bacteria and reported variations in Fe isotope ratios. The authors proposed two mechanisms of Fe fractionation to explain the isotopically light Fe observed in the soils at SPVF: Fe fractionation upon reductive dissolution in ridgetop and midslope soils with no fractionation upon reprecipitation as secondary Fe oxides at the valley floor, or no fractionation upon mobilization upslope but subsequent fractionation upon precipitation as Fe oxides in the valley. Our fixed-potential electrode results support mechanism 2 in that they emphasize fast Fe redox cycling at SPVF and little redox activity at the midslope position. It thus may be likely that Fe colloids or organically bound Fe mobilized from the midslope position are not isotopically distinct from the source rock, but after they are mobilized downslope, they are fractionated upon precipitation as Fe minerals in the valley floor (Yesavage et al. 2012).

Also based on previous work at Shale Hills, Herndon et al. (2011, 2014) and Kraepiel et al. (2015) documented active Mn cycling facilitated by tree uptake. Those researchers showed evidence that roots take up reduced Mn after reductive dissolution in the soil, and that this reduced Mn is eventually deposited on the soil surface in leaf litter. As that leaf litter decomposes and moves deeper in the soil profile, the Mn in the litter becomes more oxidized. Our results show that this Mn enrichment relative to the topsoil results in a pool of soil Mn that undergoes fast rates of redox cycling.

3D ERT reveals importance of soil morphology to spatial distribution of redox conditions

While the 3D ERT established the soil moisture conditions surrounding the electrodes over the monitoring period in 2020, it also illustrates the spatial heterogeneity of the soils of SPVF. Even though the 100-mV and 400-mV electrodes were separated by about a meter and were at the same hillslope position, the 3D ERT indicates that the 100-mV electrodes were consistently associated with higher resistivity than the 400-mV electrodes. This relatively higher resistivity could result from dense tree roots or a greater proportion of rock fragments relative to soil in that region (Garré et al. 2011; Carrière et al. 2020).

These differences in soil conditions, in part, could explain why there was a consistently negative current at 100-mV (representing oxidation of Fe), while the 400-mV electrode fluctuated often between negative

and positive currents (representing Mn reduction–oxidation cycling). We expected that the 400-mV electrode would indicate oxidizing and reducing conditions more frequently than the 100 mV in an upland soil because 400 mV is higher on the "redox ladder" (Fiedler et al. 2007). However, over periods of prolonged positive currents at 400 mV, 100 mV still only measured as oxidizing at a negative current. A soil with more coarse fragments, as suggested by the 3D ERT, could explain this departure from expectations. A rockier soil would facilitate both drainage of porewaters and downward diffusion of O_2 from the surface (Renault and Stengel 1994). Future work should include replicate electrodes fixed at the same potential and installed at the same depth to elucidate the role of such subsurface heterogeneity. At least three working electrodes fixed at the same potential should be installed at the same depth to control for some of the subsurface heterogeneity we observed through our ERT surveys.

Furthermore, ERT coupled with fixed-potential electrode measurements could be used to expand the spatial extent of the oxidation and reduction rates we measured. For example, resistivity measurements could be made daily during the monitoring period, and a model could be developed to establish a relationship between average resistivity at the location of the electrodes and the average current measured by the fixed-potential electrodes during the day of measurement. The modeled relationship between resistivity and current could then be used to infer the oxidation or reduction rate of analytes of interest across the entire ERT transect. This method would be a means to extend the measurement reach of the fixed-potential electrodes without the disturbance to soil structure caused by deployment of an array of fixed-potential electrodes.

The role of precipitation, soil moisture, and water table fluctuations in metal redox

As established by previous work at Shale Hills (Hodges et al. 2019a) and in other humid systems (Fuss et al. 2010; Knorr 2013; Hodges et al. 2018, 2019b), our study clearly demonstrates the role of soil moisture in generating reducing conditions in upland soils. The difference in redox activity between 2019 and 2020 can be explained by the differences in water table level between the two years. In 2019 there was more precipitation and the water table fluctuated between 100 and 50 cm below land surface throughout the 2-month monitoring period, while in 2020 there was less precipitation and the water table mostly remained below 1 m. Consequently, in 2019, we observed redox activity at both the 50- and 70-cm electrodes set at 100 mV. In 2020 there was no activity at 50 cm; at 70 cm we recorded only oxidation at the 100-mV electrode and fluctuating currents at the 400-mV electrode. We would anticipate reduction at 400 mV before reduction at 100 mV, due to the differences in thermodynamic favorability (Fielder et al. 2007). Therefore, these 2020 results point to less-reducing soil conditions due to lower soil moisture in 2020 than in 2019. The prolonged oxidation we recorded at 100 mV in fall 2019 supports our hypothesis that reduced species remain in porewaters over the late fall and winter. As soils dry out in the spring and summer, they then are a sink for diffusing O_2.

Clearly, soil moisture played a key role in sustaining the low-oxygen concentrations necessary for reducing conditions, especially at the 100 mV redox potential. However, precipitation events and the fluctuating water table also likely play a role in the delivery of terminal electron acceptors and electron donors to the subsurface of SPVF. Others at Shale Hills have developed a conceptual model of subsurface lateral flow paths above the regional water table that deliver precipitation that infiltrates the hillslopes of Shale Hills and flows to the subsurface of the valley, including SPVF (Lin et al. 2006; Jin et al. 2011; Yesavage et al. 2012). This depth of mixing of relatively young lateral flow with the older regional groundwater varies in depth but occurs at some points of the year within the B horizon of SPVF. Results from these past studies suggest that this lateral flowpath may have delivered colloids or organically bound Fe^{3+} from the well-drained ridgetop and midslope soils to the subsurface of SPVF, where it was subsequently reduced at the 70-cm electrode. Then, the rising water table delivered Fe^{+2} in the groundwater to the 50-cm electrode, where it was oxidized upon exposure to O_2.

Significance and conclusions

Our results provide reaction-specific confirmation of the seasonal Fe and Mn redox cycling hypothesis for the Shale Hills Watershed (Hodges et al. 2019a); metals become reduced during the growing season

when demand for O_2 is high and soils are warm and wet after rainfall events. The reduced metals remain in small pore domains and oxidize upon exposure to O_2 as soils dry following leaf-out in the late spring (Hodges et al. 2019a). The fixed-potential electrode measurements indicated predominant oxidation of reduced Fe in porewaters during the beginning of the growing season. For the first time, we demonstrate that fixed-potential electrodes may be used to track in situ redox fluctuations in moderately well-drained soils. To our knowledge, these measurements provide the most accurate real-time rates of electron transfer in an upland soil.

Indirect measures like redox potential (Eh) electrodes, passive electrodes, dyes, and infrequent measurements of reduced species in porewaters are the most common methods for tracking anaerobic respiration and reducing conditions in soils (Castenson and Rabenhorst 2006; Rabenhorst et al. 2009; Stiles et al. 2010; Dorau and Mansfeldt 2016; Hodges et al. 2018). Fixed-potential electrodes are a useful complement to such methods so that rather than redox *potential*, actual redox reactions are quantified, given the substrates available in situ. However, the rates and extents of oxidation or reduction calculated from the currents measured by the fixed-potential electrodes should be considered an estimate. The electrodes are not selective in the species with which they exchange electrons. Therefore, the measured currents generate a maximum estimate of rate and extent of a given redox reaction at that set potential. Furthermore, electron exchange with metals like Fe and Mn occurs across a range of redox potentials (not just 100 and 400 mV), and so fixed-potential electrodes do not capture the full extent of redox reactions in which an element of interest takes part. Additionally, soil pH, in part, determines the redox activity of metals at a set redox potential and so the dominant reactions at the electrode may change over the course of a deployment. Future studies could better constrain these limitations by simultaneously measuring soil pH and Eh with a fixed-potential electrode deployment to identify the likely electron exchange reactions that match with the recorded currents at the set potential.

In addition to serving as important indicators of the drainage status of a soil, Fe and Mn redox often control the fate and biogeochemical cycling of C, P, and trace metals in soils and sediments (Borch et al. 2009; Henderson et al. 2012; Herndon et al. 2017; Ma et al. 2020). Arrays of fixed-potential electrodes, when coupled with environmental monitoring of dissolved C and other constituents, could better constrain the spatial and temporal dynamics of such reactions. Furthermore, electrodes fixed at other redox potentials in soils could provide real-time rates of denitrification, sulfate reduction, or methanogenesis. Studies of reductive dissolution and subsequent mobilization of metal oxide coprecipitates, oxidative decomposition of organic carbon by reactive intermediaries, and use of alternate terminal electron acceptors in soils could benefit from the data provided by fixed-potential electrode arrays.

Acknowledgements Financial Support was provided by National Science Foundation grant EAGER SITS -1841568 to SLB, National Science Foundation Grant EAR—1331726 (SLB) for the Susquehanna Shale Hills Critical Zone Observatory, and United States Department of Agriculture Grant #2020-67034-31716 to CH. Logistical support and/or data were provided by the NSF-supported Susquehanna Shale Hills Critical Zone Observatory. This research was conducted in Penn State's Stone Valley Forest, which is funded by the Penn State College of Agriculture Sciences, Department of Ecosystem Science and Management and managed by the staff of the Forestlands Management Office. The authors thank Jeremy Harper for assistance in the field and Brosi Bradley for field and laboratory assistance.

Author contributions All authors contributed to the study conceptualization and design. Caitlin Hodges, Brandon Forsythe, and David Oakley collected the electrode and resistivity measurements. Data analysis and the first draft of the manuscript were completed by Caitlin Hodges. All authors commented on and contributed to previous versions of this manuscript. All authors read and approved the final manuscript.

Funding NSF EAR—1331726 to SLB, NSF EAGER SITS-1841568 to SLB, and USDA NIFA #2020-67034-31716 to CH.

Data availability All water table depth, soil moisture, soil gas concentration, precipitation, electrical resistivity tomography, and soil moisture datasets are publicly available under Shale Hills Time Series at http://www.czo.psu.edu/data_time_series.html.

Declarations

Competing interests The authors have no relevant financial or non-financial interests to disclose.

References

Angert A, Yakir D, Rodeghiero M et al (2015) Using O_2 to study the relationships between soil CO_2 efflux and soil respiration. Biogeosciences 12:2089–2099. https://doi.org/10.5194/bg-12-2089-2015

Brantley SL, Jin L, Andrews D, Holmes G, Bhatt M, Holleran M, Kaiser N, Williams JZ, Herndon E, Sullivan PL (2013b) Susquehanna shale hills critical zone observatory porewater chemistry (2009), Version 1.0. Interdisciplinary Earth Data Alliance (IEDA). https://doi.org/10.1594/IEDA/100236. accessed 19 oct 2022

Brantley SL, Bazilevskaya E, Andrews D, Williams JZ, Herndon E, Holmes G, Bhatt M, Holleran M, Yesavage T, Thomas E, Sullivan PL (2013c) Susquehanna Shale Hills Critical Zone Observatory Porewater Chemistry (2010), Version 1.0. Interdisciplinary Earth Data Alliance (IEDA). https://doi.org/10.1594/IEDA/100237. accessed 19 oct 2022

Borch T, Kretzschmar R, Kappler A (2009) Biogeochemical redox processes and their impact on contaminant dynamics. Environ Sci Technol. https://doi.org/10.1021/es9026248

Brantley SL, Jin L, Andrews D, Holmes G, Holleran M, Williams JZ, Herndon E, Sullivan PL (2013a) Susquehanna Shale Hills Critical Zone Observatory Porewater Chemistry (2008), Version 1.0. Interdisciplinary Earth Data Alliance (IEDA). 1**0.1594/IEDA/100235. accessed 19 oct 2022

Brantley SL, DiBiase RA, Russo TA, Shi Y, Lin H, Davis KJ, Arthur DK (2016) Designing a suite of measurements to understand the critical zone. Earth Surface Dyn 4(1):211–235

Brantley SL, Holleran ME, Jin L, Bazilevskaya E (2013d) Probing deep weathering in the Shale Hills Critical Zone Observatory, Pennsylvania (USA): the hypothesis of nested chemical reaction fronts in the subsurface. Earth Surf Process 38:1280–1298. https://doi.org/10.1002/esp.3415

Brantley SL, White T, West N, et al Susquehanna Shale Hills Critical Zone Observatory: Shale Hills in the Context of Shaver's Creek Watershed. Vadose Zone J 17:0. https://doi.org/10.2136/vzj2018.04.0092

Bridgham SD, Faulkner SP, Richardson CJ (1991) Steel rod oxidation as a hydrologic indicator in wetland soils. Soil Sci Soc Am J 55:856–862. https://doi.org/10.2136/sssaj1991.03615995005500030039x

Buettner SW, Kramer MG, Chadwick OA, Thompson A (2014) Mobilization of colloidal carbon during iron reduction in basaltic soils. Geoderma 221:139–145

Caell R, Anderson M (1986) A Technique for extensive field measurement of soil anaerobism by rusting of steel rods. Forestry. https://doi.org/10.1093/forestry/59.2.129

Carrière SD, Ruffault J, Pimont F et al (2020) Impact of local soil and subsoil conditions on inter-individual variations in tree responses to drought: insights from Electrical Resistivity Tomography. Sci Total Environ 698:134247. https://doi.org/10.1016/j.scitotenv.2019.134247

Castenson KL, Rabenhorst MC (2006) Indicator of reduction in soil (IRIS) evaluation of a new approach for assessing reduced conditions in soil. Soil Sci Soc Am J 70:1222–1226

Chacon N, Silver W, Dubinsky E, Cusack D (2006) Iron reduction and soil phosphorus solubilization in humid tropical forests soils: the roles of labile carbon pools and an electron shuttle compound. Biogeochemistry. https://doi.org/10.1007/s10533-005-2343-3

Chambers RM, Odum WE (1990) Porewater oxidation, dissolved phosphate and the iron curtain. Biogeochemistry 10(1):37–52

DeAngelis K, Silver W, Thompson AW, Firestone MK (2010) Microbial communities acclimate to recurring changes in soil redox potential status. Environ Microbiol. https://doi.org/10.1111/j.1462-2920.2010.02286.x

De-Campos AB, Huang CH, Johnston CT (2012) Biogeochemistry of terrestrial soils as influenced by short-term flooding. Biogeochemistry 111(1):239–252

Dorau K, Mansfeldt T (2015) Manganese-oxide-coated redox bars as an indicator of reducing conditions in soils. J Environ Qual 44:696–703

Dorau K, Mansfeldt T (2016) Manganese and iron oxide-coated redox bars as a tool to in situ study the element sorption in wet soils. J Soils Sediments 16:976–986. https://doi.org/10.1007/s11368-015-1300-6

Fiedler S, Vepraskas MJ, Richardson JL (2007) Soil redox potential: importance, field measurements, and observations. Adv Agron 94:1–54

Friedman E, Miller K, Lipson D, Angenent L (2013) Potentiostatically poised electrodes mimic iron oxide and interact with soil microbial communities to alter the biogeochemistry of Arctic peat soils. Mineral-Basel 3:318–336. https://doi.org/10.3390/min3030318

Friedman ES, McPhillips LE, Werner JJ et al (2016) Methane emission in a specific riparian-zone sediment decreased with bioelectrochemical manipulation and corresponded to the microbial community dynamics. Front Microbiol 6:1523. https://doi.org/10.3389/fmicb.2015.01523

Friedman ES, Rosenbaum MA, Lee AW et al (2012) A cost-effective and field-ready potentiostat that poises subsurface electrodes to monitor bacterial respiration. Biosens Bioelectron 32:309–313. https://doi.org/10.1016/j.bios.2011.12.013

Fuss CB, Driscoll CT, Johnson CE et al (2010) Dynamics of oxidized and reduced iron in a northern hardwood forest. Biogeochemistry 104:103–119. https://doi.org/10.1007/s10533-010-9490-x

Garré S, Javaux M, Vanderborght J et al (2011) Three-dimensional electrical resistivity tomography to monitor root zone water dynamics. Vadose Zone J 10:412–424. https://doi.org/10.2136/vzj2010.0079

Gosset J, Wright A (2017) Data Carpentry Python Ecology Lesson. In: Version 2017.04.0

Hall S, Silver W (2015) Reducing conditions, reactive metals, and their interactions can explain spatial patterns of surface soil carbon in a humid tropical forest. Biogeochemistry. https://doi.org/10.1007/s10533-015-0120-5

Henderson R, Kabengi N, Mantripagada N et al (2012) Anoxia-induced release of colloid-and nanoparticle-bound phosphorus in grassland soils. Environ Sci Technol. https://doi.org/10.1021/es302395r

Herndon E, AlBashaireh A, Singer D et al (2017) Influence of iron redox cycling on organo-mineral associations in Arctic tundra soil. Geochim Cosmochim Acta 207:210–231. https://doi.org/10.1016/j.gca.2017.02.034

Herndon EM, Dere AL, Sullivan PL et al (2015) Landscape heterogeneity drives contrasting concentration–discharge relationships in shale headwater catchments. Hydrol Earth Syst Sc 19:3333–3347. https://doi.org/10.5194/hess-19-3333-2015

Herndon EM, Jin L, Brantley SL (2011) Soils reveal widespread manganese enrichment from industrial inputs. Environ Sci Technol 45:241–247. https://doi.org/10.1021/es102001w

Herndon EM, Martínez CE, Brantley SL (2014) Spectroscopic (XANES/XRF) characterization of contaminant manganese cycling in a temperate watershed. Biogeochemistry 121:505–517. https://doi.org/10.1007/s10533-014-0018-7

Hodges C, Brantley SL, Sharifironizi M et al (2021) Soil carbon dioxide flux partitioning in a calcareous watershed with agricultural impacts. J Geophys Res Biogeosci. https://doi.org/10.1029/2021jg006379

Hodges C, Kim H, Brantley SL, Kaye J (2019a) Soil CO_2 and O_2 concentrations illuminate the relative importance of weathering and respiration to seasonal soil gas fluctuations. Soil Sci Soc Am J. https://doi.org/10.2136/sssaj2019.02.0049

Hodges C, King E, Pett-Ridge J, Thompson A (2018) Potential for iron reduction increases with rainfall in montane basaltic soils of Hawaii. Soil Sci Soc Am J 82:176. https://doi.org/10.2136/sssaj2017.06.0193

Hodges C, Mallard J, Markewitz D et al (2019b) Seasonal and spatial variation in the potential for iron reduction in soils of the Southeastern Piedmont of the US. CATENA 180:32–40. https://doi.org/10.1016/j.catena.2019.03.026

Huang W, Hall SJ (2017) Optimized high-throughput methods for quantifying iron biogeochemical dynamics in soil. Geoderma 306:67–72. https://doi.org/10.1016/j.geoderma.2017.07.013

Hunter JD (2007) Matplotlib: a 2D graphics environment. Comput Sci Eng 9:90–95. https://doi.org/10.1109/MCSE.2007.55

Jin L, Andrews DM, Holmes GH et al (2011) Opening the "Black Box": water chemistry reveals hydrological controls on weathering in the susquehanna shale hills critical zone observatory. Vadose Zone J 10:928. https://doi.org/10.2136/vzj2010.0133

Jin L, Ravella R, Ketchum B et al (2010) Mineral weathering and elemental transport during hillslope evolution at the Susquehanna/Shale Hills Critical Zone Observatory. Geochim Cosmochim Ac 74:3669–3691. https://doi.org/10.1016/j.gca.2010.03.036

Jones ME, Nico PS, Ying SC et al (2018) Manganese-driven carbon oxidation at oxic-anoxic interfaces. Environ Sci Technol. https://doi.org/10.1021/acs.est.8b03791

Kim H, Stinchcomb G, Brantley SL (2017) Feedbacks among O2 and CO2 in deep soil gas, oxidation of ferrous minerals, and fractures: a hypothesis for steady-state regolith thickness. Earth Planet Sci Lett. 460:29–40. https://doi.org/10.1016/j.epsl.2016.12.003

K-HKnorr2013DOC-dynamics in a small headwater catchment as driven by redox fluctuations and hydrological flow paths–are DOC exports mediated by iron reduction/oxidation cycles?Biogeosciences10.5194/bg-10-891-2013Knorr K-H (2013) DOC-dynamics in a small headwater catchment as driven by redox fluctuations and hydrological flow paths–are DOC exports mediated by iron reduction/oxidation cycles? Biogeosciences. https://doi.org/10.5194/bg-10-891-2013

Kraepiel AML, Dere AL, Herndon EM, Brantley SL (2015a) Natural and anthropogenic processes contributing to metal enrichment in surface soils of central Pennsylvania. Biogeochemistry. https://doi.org/10.1007/s10533-015-0068-5

Lin H, Kogelmann W, Walker C, Bruns M (2006) Soil moisture patterns in a forested catchment: a hydropedological perspective. Geoderma 131:345–368

Linkhorst A, Dittmar T, Waska H (2016) Molecular fractionation of dissolved organic matter in a shallow subterranean estuary: the role of the iron curtain. Environ Sci Technol. https://doi.org/10.1021/acs.est.6b03608

Lipson D, Jha M, Raab T, Oechel WC (2010) Reduction of iron(III) and humic substances plays a major role in anaerobic respiration in an Arctic peat soil. J Geophys Res. https://doi.org/10.1029/2009JG001147

Logan BE, Rossi R, Ragab A, Saikaly PE (2019) Electroactive microorganisms in bioelectrochemical systems. Nat Rev Microbiol 17:307–319. https://doi.org/10.1038/s41579-019-0173-x

Lovley DR, Phillips EJ (1988) Novel mode of microbial energy metabolism: organic carbon oxidation coupled to dissimilatory reduction of iron or manganese. Appl Environ Microbiol 54:1472–1480

Ma D, Wu J, Yang P, Zhu M (2020) Coupled manganese redox cycling and organic carbon degradation on mineral surfaces. Environ Sci Technol 54:8801–8810. https://doi.org/10.1021/acs.est.0c02065

McKinney W (2010) Data Structures for Statistical Computing in Python. In: Walt S van der, Millman J (eds) Proceedings of the 9th Python in Science Conference. pp 56–61

Michot D, Benderitter Y, Dorigny A et al (2003) Spatial and temporal monitoring of soil water content with an irrigated corn crop cover using surface electrical resistivity tomography: soil water study using electrical resistivity. Water Resour Res. https://doi.org/10.1029/2002wr001581

Owens P, Wilding L, Miller W, Griffin R (2008) Using iron metal rods to infer oxygen status in seasonally saturated soils. CATENA 73:197–203

Pandas Development Team (2020) pandas-dev/pandas: Pandas. Version latest. Zenodo. https://doi.org/10.5281/zenodo.3509134

Pett-Ridge J, Silver WL, Firestone MK (2006) Redox fluctuations frame microbial community impacts on N-cycling rates in a humid tropical forest soil. Biogeochemistry 81:95–110. https://doi.org/10.1007/s10533-006-9032-8

Rabenhorst M, Hively W, James B (2009) Measurements of soil redox potential. Soil Sci Soc Am J 73:668–674

Rabenhorst MC, Burch S (2006) Synthetic iron oxides as an indicator of reduction in soils (IRIS). Soil Sci Soc Am J 70:1227–1236

Renault P, Stengel P (1994) Modeling oxygen diffusion in aggregated soils: I. Anaerobiosis inside the aggregates. Soil Sci Soc Am J 58(4):1017–1023

Roden EE, Kappler A, Bauer I, Jiang J, Paul A, Stoesser R, Konishi H, Xu H (2010) Extracellular electron transfer through microbial reduction of solid-phase humic substances. Nat Geosci 3(6):417–421. https://doi.org/10.1038/ngeo870

Samouëlian A, Cousin I, Tabbagh A, Bruand A, Richard G (2005) Electrical resistivity survey in soil science: a review. Soil Tillage Res 83(2):173–193

Sander M, Hofstetter TB, Gorski CA (2015) Electrochemical analyses of redox-active iron minerals: a review of nonmediated and mediated approaches. Environ Sci Technol 49(10):5862–5878

Schaetzl RJ, Rothstein DE (2016) Temporal variation in the strength of podzolization as indicated by lysimeter data. Geoderma 282:26–36. https://doi.org/10.1016/j.geoderma.2016.07.005

Scott B, Baldwin AH, Yarwood S et al (2021) Macro and microscopic visual imaging tools to investigate metal reducing bacteria in soils. Soil Sci Soc Am J 85:184–192. https://doi.org/10.1002/saj2.20171

Shelobolina E, Konishi H, Xu H, Benzine J, Xiong MY, Wu T, Blöthe M, Roden E (2012) Isolation of phyllosilicate-iron redox cycling microorganisms from an illite-smectite rich hydromorphic soil. Front Microbiol 3:134. https://doi.org/10.3389/fmicb.2012.00134

Stiles CA, Dunkinson ET, Ping C, Kidd J (2010) Initial field installation of manganese indicators of reduction in soils, Brooks Range, Alaska. Soil Surv Horizons 51:102–107

Stumm W, Morgan JJ (1996) Aquatic chemistry: chemical equilibria and rates in natural waters. Wiley

Viollier E, Inglett PW, Hunter K et al (2000) The ferrozine method revisited: Fe(II)/Fe(III) determination in natural waters. Appl Geochem 15:785–790. https://doi.org/10.1016/s0883-2927(99)00097-9

Virtanen P, Gommers R, Oliphant TE et al (2020) SciPy 1.0: fundamental algorithms for scientific computing in Python. Nat Methods 17:261–272. https://doi.org/10.1038/s41592-019-0686-2

Waskom ML (2021) seaborn: statistical data visualization. J Open Source Softw 6:3021. https://doi.org/10.21105/joss.03021

Weitzman JN, Kaye JP (2018) Nitrogen budget and topographic controls on nitrous oxide in a shale-based watershed. J Geophys Res Biogeosci 123(6):1888–1908

Yesavage T, Fantle MS, Vervoort J et al (2012) Fe cycling in the Shale Hills Critical Zone Observatory, Pennsylvania: an analysis of biogeochemical weathering and Fe isotope fractionation. Geochim Cosmochim Acta 99:18–38

Zausig J, Stepniewski W, Horn R (1993) Oxygen concentration and redox potential gradients in unsaturated model soil aggregates. Soil Sci Soc Am J 57(4):908–916